Chemical Engineering Journal 509 (2025) 161070

Contents lists available at ScienceDirect

Chemical Engineering Journal

journal homepage: www.elsevier.com/locate/cej

Defect-rich FeCoNiMnRu high-entropy alloys with activated interfacial water for boosting alkaline water/seawater hydrogen evolution

Guangbo Liu [a], Chen Song [a], Xiaolei Li [a], Qisen Jia [a], Pengfei Wu [a], Zhihao Lou [a], Yuanshuo Ma [a], Xuejing Cui [a], Xin Zhou [b,c,**], Luhua Jiang [a,*]

[a] College of Materials Science and Engineering, Qingdao University of Science and Technology, Qingdao 266042, PR China
[b] Interdisciplinary Research Center for Biology and Chemistry, Liaoning Normal University, Dalian 116029, PR China
[c] College of Environment and Chemical Engineering, Dalian University, Dalian 116622, PR China

ARTICLE INFO

Keywords:
Defect-rich
High-entropy alloy
Hydrogen evolution reaction
Interfacial water
In-situ FTIR

ABSTRACT

Water molecules are the most important participant in hydrogen evolution reaction (HER) under alkaline water/seawater conditions, while effectively activating the rigid interfacial water and promoting the HER kinetics remain a great challenge. Herein, we construct a defect-rich FeCoNiMnRu high-entropy alloy (HEA) by rapid Joule-heating approach, which could significantly reform the structure and dynamics of interfacial water and consequently boost the HER activity. In-situ Fourier transform infrared (FTIR) spectra and ab initio molecular dynamics (AIMD) calculations confirm that the constructed FeCoNiMnRu HEA endows a fast conversion of interfacial water from strong H-bonded water to free water, which increases the availability and activity of H_2O^* at the active sites, and thereby facilitating the HER process. Consequently, the developed defect-rich FeCoNiMnRu HEA exhibits excellent activity with overpotentials of only 37 and 35 mV at 10 mA cm^{-2} in alkaline water and seawater electrolytes, respectively, which are surpassing that of commercial Pt/C. This work discloses the behavior and structure of interfacial water on HEA and provides new insights into the design of advanced HEA-based catalysts towards HER.

1. Introduction

Alkaline water/seawater electrolysis driven by renewable energies well meets the demands for large-scale and sustainable production of green hydrogen, which has attracted great attentions in recent years [1]. To catalyze the hydrogen evolution reaction (HER) in water/seawater electrolysis systems efficiently, developing advanced electrocatalysts is of vital importance [2–4]. To this end, intensive studies have been focused on the catalyst design and revelation of structure-HER activity over the past decades, as such, various HER catalysts including noble/non-noble metals and composites, metal oxides, phosphides, chalcogenides, carbides, nitrides, and metal-free materials have been developed accordingly [2,3,5–9]. Among these developed catalysts, high-entropy alloys (HEAs) have been attracted special attention due to the following reasons: (1) HEAs have distinctive characteristics, like high-entropy effect, lattice distortion effect, sluggish diffusion, and the “cocktail’’ effect, which can enhance the performance of catalysts from multiple aspects. (2) HEAs have complex surface structures and tunable compositions, which can optimize catalytic active sites and thereby enhance the efficiency of HER. (3) Due to their multi-element composition, HEAs possess high thermodynamic stability and corrosion resistance, enabling them to maintain long-term stable operation in the harsh environment of seawater electrolysis. (4) Compared with traditional noble-metal catalysts (such as Pt and Ir), HEAs have lower raw material costs and are more abundant in resources, making them more suitable for large-scale industrial applications [10–12]. Consequently, numerous HEA-based materials with diverse compositions and structures have been successfully constructed and applied to HER in alkaline water/seawater conditions [13–15]. Nowadays, the HER mechanisms related to electron transfer, water adsorption/dissociation, and intermediates adsorption/desorption behaviors of HEAs have been well understood in both experimental and theoretical researches [12,16,17]. Nevertheless, interfacial water as the most important participant in HER, the fundamental insight into the structure and behavior of interfacial water on the surface of HEAs during HER remains obscure and needs better understanding.

---

[*] Corresponding author.
[**] Corresponding author.
E-mail addresses: zhouxin@dlu.edu.cn (X. Zhou), luhuajiang@qust.edu.cn (L. Jiang).

https://doi.org/10.1016/j.cej.2025.161070
Received 22 December 2024; Received in revised form 9 February 2025; Accepted 25 February 2025

Recently, pioneer researchers have verified that the interfacial water on the catalyst surface plays a critical role in the HER process. For instance, Li and Pan et al. demonstrated that the interfacial water with more ordered structure at the electrolyte/catalyst interface could facilitate the electron transfer across the interface and lead to higher HER activity [18]. Jiang et al. investigated the ion-specific water structures with different alkali metal cations, and revealed that the interfacial water could form an ordered structure with Li^+ cations while distorted structure with Cs^+/K^+ cations, thus leading to cation-dependent HER kinetics [19]. Chen group found that the interfacial water has more connective H-bond networks in acidic electrolyte than that of alkaline electrolyte, which intrinsically accounts for the fast kinetics of acidic HER [20]. In other studies, Zhang and co-workers discovered that FeNiRu/C with a short-range ordered Turing structure could optimize the interfacial water structure and help to transform strong H-bonded water to more free water, thereby facilitating the water dissociation [21]. Chen et al. [22] and Pan et al. [23] confirmed that disordering the interfacial water network could promote the transport of H_2O^*/OH^* and increase the availability of H_2O^*, thus leading to the enhanced HER activity.

In brief, current researches reveal that different electrolyte/catalyst interfaces could affect the structure of interfacial water, which consequently impact the HER kinetics and efficiency significantly. As for HEAs, the understanding of their HER mechanisms remains in the conventional structure–activity relationships that established earlier. Given water molecules are the dominant reactant and proton donors for HER in alkaline conditions, the availability and activity of interfacial water at the electrode surface is vital important for boosted HER activity [20,24–26]. Therefore, unraveling the structure and behavior of interfacial water on the surface of HEAs would allow for building the structure-interfacial water relationships and interfacial water-HER activity relationships of HEA-based materials, which are yet to be established.

Herein, we for the first time construct a defect-rich FeCoNiMnRu HEA by rapid Joule-heating approach, and investigate the role of interfacial water on the HEA surface and the consequent relevance to HER activity in alkaline water/seawater media. In-situ Fourier transform infrared (FTIR) spectra and ab initio molecular dynamics (AIMD) results reveal that the FeCoNiMnRu HEA could effectively regulate the structure of interfacial water, endowing the fast conversion of interfacial water from strong H-bonded water to free water, and thereby accelerating the transport of H_2O^*/OH^* and increasing the amount of available H_2O^* to the active sites. Functional density functional theory (DFT) calculations further demonstrate that more stabilized intermediates (H_2O^*/OH^*) and moderated H* adsorption are achieved on FeCoNiMnRu HEA, confirming the high theoretical intrinsic HER activity. As demonstrated experimentally, the developed defect-rich FeCoNiMnRu HEA deliver superior HER activity in both alkaline water and seawater electrolytes with overpotentials of only 37 and 35 mV at 10 mA cm^{-2}, respectively, surpassing commercial Pt/C.

2. Experimental section

2.1. Synthesis of carbon nanofiber support

The carbon nanofiber (CNF) support was synthesized by electrospinning technique and subsequent carbonization treatment process. Firstly, 12.8 g polyacrylonitrile (PAN) were dissolved in 100 mL of dimethyl formamide (DMF) to form a concentration of 12 wt% precursor solution. Secondly, the obtained precursor solution were assembled to the electrospinning machine and electrospinning into PAN fibers with a spinning distance of 15 cm, and a feed rate of 0.4 mL h^{-1} at a voltage of 22 kV. After that, PAN fibers were carbonized to create the CNF support after pre-oxidation at 260 ℃ for 5 h in muffle furnace and subsequent carbonization treatment at 1100 ℃ for 2 h in a quartz tube furnace.

2.2. Synthesis of FeCoNiMnRu HEAs

The CNF support was washed successively with acetone, ethanol and deionized water for 10 min and dried in an oven. After that, the FeCoNiMnRu precursor solution was prepared by dissolving 0.5 mmol $CoCl_2·6H_2O$, $NiCl_2·6H_2O$, $FeCl_3·6H_2O$, $MnCl_2·4H_2O$ and 0.05 mmol $RuCl_3·xH_2O$ in a mixture of ethanol (3.64 mL) and deionized water (1.36 mL), resulting in a standard concentration of 0.1 mol L^{-1}. Then, 72 μL of the standard precursor solution was drop-cast onto the CNF (0.6 × 1 cm^2) and dried in an oven. Finally, the CNF was heated through Joule heating apparatus (Hefei In-situ Technology Co., Ltd.) with 0.5 s thermal shock at ~ 1000℃ in vacuum. With the same method, FeCoNi, FeCoNiMn and FeCoNiRu were synthesized. For comparison, FeCoNiMnRu samples with different precursor solution concentrations (0.025, 0.045, 0.065 and 0.085 mol L^{-1}) were also prepared.

2.3. Materials characterization

X-ray diffraction (XRD) patterns of the samples were obtained on a Rigaku D-max-γ X-ray diffractometer with Cu-Kα X-ray radiation (λ = 1.5418 Å). Scanning electron microscopy (SEM) images were taken by using a JEOL JSM-6700F field-emission scanning electron microscope (FE-SEM). Transmission electron microscope (TEM), high-resolution TEM (HRTEM), high-angle annular dark field (HAADF) images and energy dispersive X-ray spectroscopy (EDS) were performed on a JEOL JEM-2100 transmission electron microscopy. X-ray photoelectron spectroscopy (XPS) spectra were carried out on a Thermo Scientific ESCALab250Xi using monochromated Al Kα radiation. Inductively coupled plasma optical emission spectrometry (ICP-OES) was carried out on an Agilent 7800 instrument. In-situ Fourier transform infrared (FTIR) spectroscopy experiments were conducted using a Thermo iS20 spectrometer equipped with an MCT detector and an in situ reaction cell (Hefei In-situ Technology Co., Ltd.).

2.4. Electrochemical measurements

The electrochemical measurements were accomplished with a conventional three-electrode system controlled using a CHI760E electrochemical work station (CH Instruments Ins.). The as-prepared samples were used as the working electrode, a Hg/HgO electrode and a graphite rod were served as the reference and counter electrode, respectively. To prepare the reference Pt/C working electrode, 5 mg commercial 20 wt% Pt/C and 1 mg carbon black were dispersed in 1970 μL ethanol and 30 μL Nafion solution (5 wt%) with ultrasonic treatment for 30 min to form a uniform suspension. Then, 50 μL of the catalyst suspension was gently pipetted onto the NF (0.5 × 1 cm^2) and dried naturally. The drop-coating operation repeated twice and finally lead to a catalyst loading of 0.25 mg cm^{-2}.

The HER performances were investigated in alkaline (1.0 M KOH) and alkaline seawater (1.0 M KOH + 0.5 M NaCl) solutions. All potentials were iR-corrected and converted to potentials vs. the reversible hydrogen electrode (RHE) using equation: E (vs. RHE) = E (vs. Hg/HgO) + 0.0592 × pH + 0.098. Linear sweep voltammetry (LSV) curves with scan rate of 5 mV s^{-1} were recorded after purging with high-purity N_2 gas for 30 min. Electrochemical impedance spectroscopy (EIS) measurements were conducted at an overpotential of 100 mV under conditions ranging from 100 kHz to 0.1 Hz. Double-layer (C_{dl}) capacitance was fitted by measuring CVs in a window without Faradaic processes at scan rates of 20, 40, 60, 80 and 100 mV s^{-1}. The electrochemical surface area (ECSA) was calculated by the equation:

$$\mathrm{ECSA} = C_{dl}/C_s \tag{1}$$

where C_s represented the specific capacitance (0.04 mF cm^{-2}). The ECSA-normalized LSV curves were acquired according to the equation: J/ECSA, where J is the geometric current density of the working electrode.

The turnover frequency (TOF) is calculated by the following equation [27]:

$$TOF(s^{-1}) = \frac{numberoftotalhydrogenturnovers/cm^2}{numberofactiveofsites/cm^2} \tag{2}$$

$$= \frac{|J|(mAcm^{-2})}{n \times 1000 \times N \times ECSA \times (1.602 \times 10^{-19}C)} = \frac{6.24 \times 10^{15} \times |J|}{n \times N \times ECSA}$$

where N is the density of active sites, n is the number of electrons involved in the reaction, which is 2 for the HER. The density of active sites can be calculated as follows:

$$N = (\frac{Number\ of\ sites/unit\ cell}{Volume/unit\ cell})^{\frac{2}{3}} \tag{3}$$

2.5. Theory calculations

Functional density functional theory (DFT) calculations were performed by the Vienna ab initio simulation package (VASP) [28,29]with the projector augmented wave (PAW) pseudopotentials.[30] The Perdew-Burke-Ernzerhof (PBE) parameterization of the generalized gradient approximation (GGA) was adopted for the exchange correlation.[31] The energy cutoff employed for plane-wave expansion was set to 400 eV. The structures of high entropy alloys (HEA) FeCoNiRu and FeCoNiRuMn were obtained using Special Quasi Random Structure (SQS) generation method from The Alloy-Theoretic Automated Toolkit (ATAT) code [32,33]. Based on the optimized bulk structures, the (111) surface for each alloy was modeled by a slab including 100 metal atoms. According to the experimental samples, there are 25 Fe atoms, 34 Co atoms, 38 Ni atoms, and 3 Ru atoms in FeCoNiRu (111) surface, and there are 21 Fe atoms, 20 Co atoms, 34 Ni atoms, 3 Ru atoms, and 12 Mn atoms in FeCoNiRuMn (111) surface. The supercells were repeated periodically on the x-y plane while a vacuum region of 15 Å was applied along the z-direction to avoid mirror interaction between adjacent supercells. Consequently, the sizes of the slabs are 24.667 Å × 17.789 Å × 17.711 Å for FeCoNiRu and 24.679 Å × 17.794 Å × 17.736 Å for FeCoNiRuMn. The Brillouin zone integration was sampled on a 1 × 1 × 1 Gamma k-point grid for structural optimization and electronic structure calculation. All atoms were relaxed until the Hellman-Feynman forces on individual atoms were less than 0.01 eV $Å^{-1}$. During the structural relaxation, the bottom two metal layers were fixed at their bulk positions and the top two metal layers and adsorbates were allowed to move.

Based on Nørskov's assumption [34], the Gibbs free energy (ΔG_H) of the hydrogen evolution reaction (HER) is calculated by

$$\Delta G_H = \Delta EH + \Delta ZPE - T\Delta S_H \tag{1}$$

ΔE_H is the hydrogen adsorption energy, obtained by $\Delta E_H = E_{H^*} - E_* - \frac{1}{2}E_{H_2}$, where E_{H^*}, E_* and E_{H_2} represent the calculated energies of the surface adsorbed with a hydrogen atom, the clean surface and the H_2 molecule in gas phase, respectively. ΔZPE is the difference in zero-point energies of three species above. The zero-point energy of pure surface can be estimated to be zero. Since the entropies of surface structures are approximate to be zero, ΔS_H is equal to the negative value of half the entropy of H_2 in the gas phase at standard conditions.

Ab initio molecular dynamics (AIMD) simulations were utilized to evaluate the thermodynamic stability of the constructed interfacial structures by means of VASP. The energy cutoff of the plane wave basis set was set to be 400 eV and the Brillouin zone was sampled at the Γ-point. The Nosé-Hoover thermostat was used to simulate the canonical ensemble with constant number of particles, volume, and temperature (NVT) [35,36]. The temperature was set to be 300 K for a time period of 1000 fs with a time step of 1 fs. The catalyst-water interface is modelled to contain 170 O atoms and 340 H atoms, giving water a density close to 1.0 g mL^{-1}.

3. Results and discussion

3.1. Characterizations of the defect-rich FeCoNiMnRu HEAs

The defect-rich FeCoNiMnRu HEAs were prepared via a rapid Joule heating synthesis procedure as illustrated in Fig. 1a. Firstly, the FeCoNiMnRu precursor solution was drop-coated on CNF support. After drying, the CNF support was fixed on a Joule heating apparatus and rapidly heated up to ~ 1000 ℃ in 0.5 s under vacuum to obtained FeCoNiMnRu HEAs (see the Experimental Section for details). In the preparing process, the heating rate and quenching rate reach up to ~ 2000 ℃ s^{-1} and ~ 2500 ℃ s^{-1} (Fig. S1), respectively, featuring a whole production cycle of only ~ 0.9 s, thus indicating the extremely-high preparation efficiency of FeCoNiMnRu HEAs. The morphology of the FeCoNiMnRu HEAs were examined by scanning electron microscopy (SEM). As shown in Fig. 1b, the resultant FeCoNiMnRu HEAs exhibit agglomerated nanoparticles in morphology and are uniformly distributed on the surface of CNF. FeCoNiMnRu HEAs prepared with different precursor solution concentrations as well as the obtained FeCoNi, FeCoNiMn and FeCoNiRu all exhibit the similar morphology (Fig. S2 and S3). Transmission electron microscopy (TEM) image further indicates that the as-prepared FeCoNiMnRu HEAs are well anchored on the CNF support with particle sizes of 5 ~ 50 nm (Fig. S4). In the high-resolution TEM (HRTEM) images of the FeCoNiMnRu HEAs (Fig. 1c and d), lattice fringes with a interplanar spacing of 0.198 nm can be determined, corresponding to the (1 1 1) planes of face-centered-cubic (FCC) structure [37]. Meanwhile, the HRTEM images uncover that many point defects and lattice distortions can be clearly observed in the obtained FeCoNiMnRu HEAs (indicated by green arrows in Fig. 1d, e and f), which are believed to stem from the unconventional nucleation and grain growth due to the rapid heating/quenching rate of Joule-heating process. To further reflect the lattice distortion and defect-rich structures of FeCoNiMnRu HEA, we carried out strain quantification by geometrical phase analyses (GPA) technique. As shown in Fig. 1g and h, the GPA results show that highly-uneven local stress and strain are distributed in the whole FeCoNiMnRu HEAs, confirming the existence of large amount of lattice distortions and defects [14,38]. Of note, the defect-rich structure of FeCoNiMnRu HEA provides more active sites for HER, which would definitely contribute to the improved electrocatalytic performance [39]. Fig. 1i presents the HAADF image and corresponding EDS elemental mappings of FeCoNiMnRu HEA, which reveal that the Fe, Co, Ni, Mn, and Ru elements are homogeneously distributed in the entire sample, confirming the successful synthesis of FeCoNiMnRu HEA. In addition, the Fe, Co, Ni, Mn, and Ru contents in the FeCoNiMnRu HEA are analyzed by ICP-OES (Fig. S5), where a stoichiometric composition of $Fe_{0.21}Co_{0.30}Ni_{0.34}Mn_{0.12}Ru_{0.03}$ is finally identified. The proportion of Ru content is only ~ 3 at.% in the FeCoNiMnRu HEA, indicating the low content and matching well with the designed composition. The loading of the FeCoNiMnRu HEA is determined to be about 0.29 mg cm^{-2} based on the ICP results.

The crystal structure of FeCoNiMnRu HEA was investigated using X-ray diffraction (XRD). As shown in Fig. 2a, due to the small nanoparticle sizes and large amount of CNF support, the XRD peaks are mainly attributed to carbon while the peaks presented in the XRD patterns of FeCoNi, FeCoNiMn, FeCoNiRu, and FeCoNiMnRu are weak and similar. The observed weak peak for all samples is located at 44.2°, which corresponds to the (111) facet of $FeNi_3$ (PDF#38–0419), indicating a FCC phase configuration within the resultant FeCoNiMnRu. Meanwhile, the calculated lattice constant for this diffraction peak is 0.203 nm, which is well in agreement with the TEM result (Fig. 1d). X-ray photoelectron spectroscopy (XPS) was then employed to investigate the composition and chemical states of FeCoNiMnRu HEA. The XPS survey spectrum reveals that except C and O elements, five metal elements of Fe, Co, Ni, Mn, and Ru are clearly identified in the FeCoNiMnRu HEA (Fig. S6), consistent with the EDS analysis result. The high-resolution XPS spectra of Fe 2p, Co 2p, Ni 2p, Mn 2p, and Ru 3p are presented in Fig. 2b-f. It is

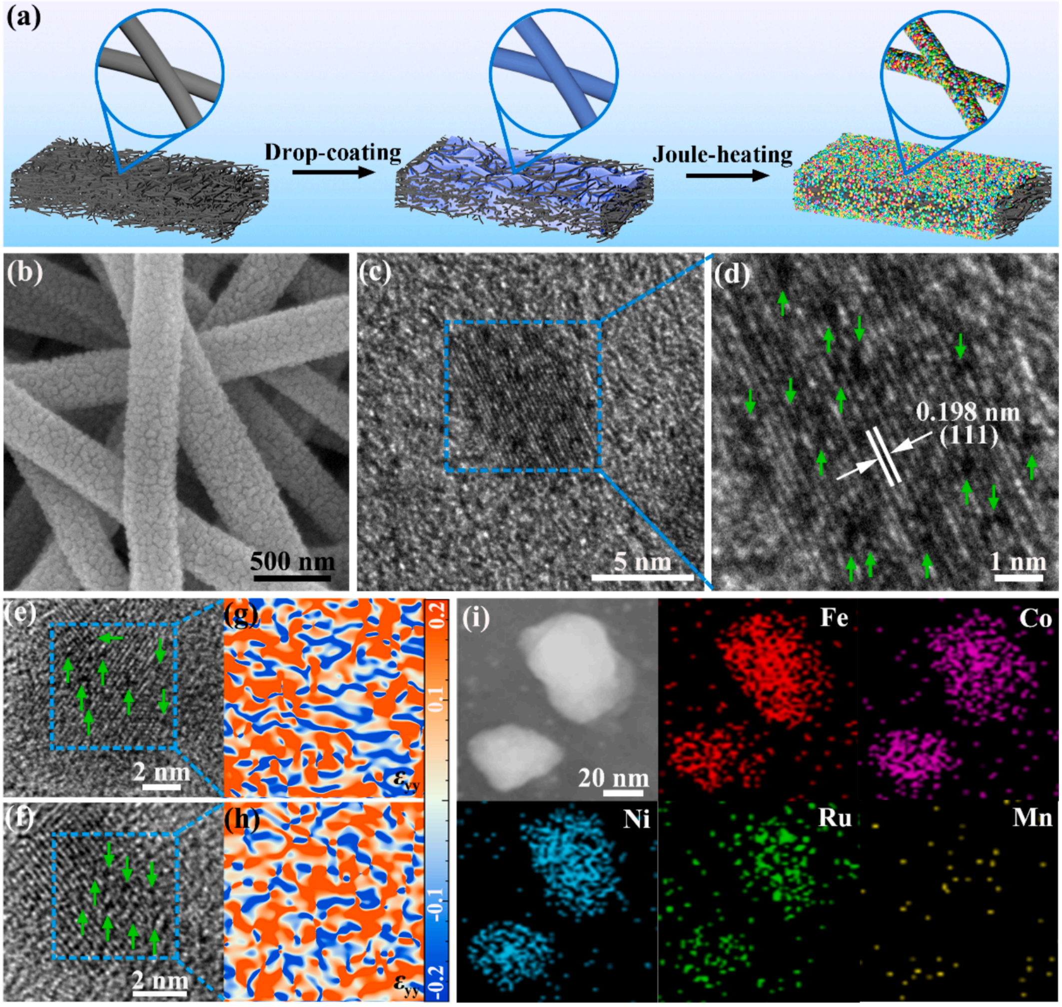

Fig. 1. (a) Schematic illustration for synthesis of FeCoNiMnRu HEA. (b) SEM, (c) HRTEM and (d) enlarged HRTEM images of FeCoNiMnRu HEA. (e, f) Typical HRTEM images and (g, h) corresponding GPA images of FeCoNiMnRu HEA. (i) HAADF image and corresponding EDS elemental mappings of FeCoNiMnRu HEA.

found that the Fe, Co, Ni and Mn elements exist in both the metallic and oxidized states while Ru element is solely in the metallic state. The coexistence of metallic and oxidized state could generate not only the synergistic effect but also the lattice distortions and defects in the FeCoNiMnRu HEA, which could promote the electron transfer and adsorption/desorption kinetics of the reactant molecule/intermediates, thus leading to enhanced electrocatalytic activity [40]. As shown in Fig. 2b, the Fe 2p XPS spectrum reveals that the Fe^0 specie is located at 707.1/717.6 eV while the Fe^{2+} and Fe^{3+} species are located at 710.0/720.3 and 712.2/723.3 eV, respectively [37]. Another two peaks located at 715.1 and 727.6 eV are attributed to the satellite peaks of Fe 2p. The Co 2p XPS spectrum shows that the Co^0, Co^{2+} and Co^{3+} species are located at 777.4/792.6, 781.8/797.5 and 779.2/794.9 eV, respectively (Fig. 2c) [13]. In the Ni 2p XPS spectrum, the peaks at 851.2 eV and 869.4 eV are assigned to the Ni^0 species. The peaks at 853.5 eV and 870.8 eV are assigned to the Ni^{2+} species, while the peaks at 855.9 eV and 873.7 eV are attributed to the Ni^{3+} species [41]. Additionally, the peaks at 861.9 and 880.1 eV are identified as satellite peaks. The high-resolution Mn 2p XPS spectrum suggests that the Mn^0 specie is observed at 638.3/650.4 eV while the Mn^{2+} and Mn^{3+} species are found at 641.6/653.1 and 643.4/654.7 eV, respectively [42]. The XPS peak appeared at 646.8 eV is attributed to the satellite signal of Mn 2p. For Ru 3p XPS spectrum, two peaks located at 462.6 and 484.3 eV can be observed, which are attributed to the metallic Ru specie [38]. For comparison, the chemical states of Fe, Co, Ni and Mn elements in FeCoNiMn were also examined (Fig. S7). It is found that the binding energies of Fe 2p, Co 2p, Ni 2p and Mn 2p in FeCoNiMn show negative shifts as compared with FeCoNiMnRu, implying the electronic interactions among metal elements in the HEAs [15]. This suggests that the electron transfers from Fe, Co, Ni and Mn to Ru in the FeCoNiMnRu HEA, which is mainly attributed to the lower electro-negativities of Fe (1.83), Co(1.88), Ni (1.91) and Mn (1.55) than that of Ru (2.20) [43]. It is believed that the electronic interaction among metal elements in the FeCoNiMnRu HEA is helpful to regulate the adsorption/desorption of the reaction intermediates, thus facilitating the HER process [13].

3.2. HER performances of FeCoNiMnRu HEA

To evaluate the HER performances of the FeCoNiMnRu HEA, electrochemical measurements were carried out using a typical three-electrode configuration in alkaline water/seawater electrolytes. The HER activities of FeCoNiMnRu HEAs prepared with different precursor solution concentrations were firstly evaluated in 1.0 M KOH electrolyte. The recorded LSV curves reveal that the FeCoNiMnRu HEA prepared with precursor solution concentration of 0.065 mol L^{-1} achieved the highest HER activity (Fig. S8). Therefore, 0.065 mol L^{-1} was chosen as the standard precursor solution concentration to prepare FeCoNiMnRu. The performances of the FeCoNi, FeCoNiMn, FeCoNiRu prepared with precursor solution concentration of 0.065 mol L^{-1} and commercial Pt/C (20 wt%) were also evaluated for comparison. The HER polarization curves of all the samples recorded in 1.0 M KOH electrolyte are presented in Fig. 3a. It is found that the FeCoNiMnRu HEA exhibits the best

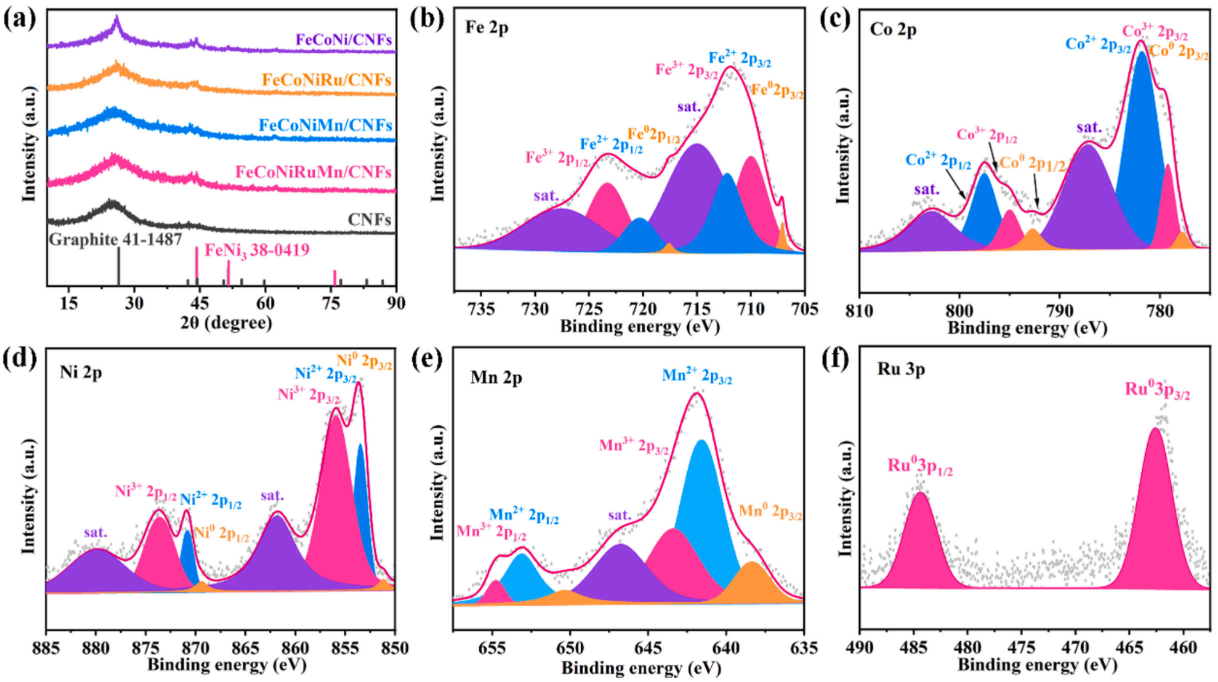

Fig. 2. (a) XRD pattern of FeCoNi, FeCoNiRu, FeCoNiMn and FeCoNiMnRu. High resolution XPS spectra of (b) Fe 2p, (c) Co 2p, (d) Ni 2p, (e) Mn 2p and (f) Ru 3p in the FeCoNiMnRu HEA.

performance toward HER among the alloys samples, which is even superior to the commercial Pt/C. As presented in Fig. 3b, the FeCoNiMnRu HEA only needs overpotentials of 32/122/170 mV to gain current densities of 10/50/100 mA cm^{-2}, much lower than those of FeCoNi (184/276/313 mV), FeCoNiRu (52/165/217 mV) and FeCoNiMn (185/325/374 mV). Meanwhile, the Tafel slope of FeCoNiMnRu HEA is calculated to be only 44 mV dec^{-1} (Fig. 3c), which is significantly lower than that of the FeCoNi (198 mV dec^{-1}), FeCoNiRu (72 mV dec^{-1}) and FeCoNiMn (207 mV dec^{-1}), and also lower than that of Pt/C (51 mV dec^{-1}), indicating the fast HER kinetics. Of note, the Tafel slope of FeCoNiMnRu HEA is located in the theoretical value range of $40 \sim 120$ mV dec^{-1}, suggesting it follows a Volmer-Heyrovsky mechanism in alkaline electrolyte [44,45]. The charge transfer kinetics at the catalyst/electrolyte interface were then probed by using electrochemical impedance spectroscopy (EIS). It is found that FeCoNiMnRu HEA reveals the smallest semicircle as compared with that of FeCoNi, FeCoNiRu and FeCoNiMn (Fig. S9), thus indicating the fastest charge transfer kinetics during HER process. Moreover, electrochemical double-layer capacitance (C_{dl}) measurements were carried out to probe the origin of the HER activity. As shown in Fig. S10, the C_{dl} of FeCoNiMnRu HEA is calculated to be 54.17 mF cm^{-2}, obviously higher than that of FeCoNi (40.21 mF cm^{-2}), FeCoNiRu (32.76 mF cm^{-2}) and FeCoNiMn (44.71 mF cm^{-2}), implying the largest electrochemically active surface area (ECSA) for HER. The larger ECSA is believed to derive from the defect-rich structure of FeCoNiMnRu HEA, which provides more active sites for adsorbing/desorbing the reactant molecule/intermediates and thereby promoting HER activity. To clarify the true HER activity, ECSA-normalized LSV curves of these HEAs were provided (Fig. S11). It is found that FeCoNiMnRu HEA delivers much higher ECSA-normalized current density than FeCoNi, FeCoNiRu and FeCoNiMn in alkaline water/seawater electrolytes, indicating the higher intrinsic activity. Additionally, turnover frequency (TOF), which is a critical metric for evaluating HER electrocatalysts [46], was further evaluated for all samples. As illustrated in Fig. S12, the FeCoNiMnRu HEA exhibits the highest TOF value among these HEAs, confirming the superior HER efficiency.

The HER activity of FeCoNiMnRu HEA was then evaluated in alkaline seawater electrolyte. The comparing LSV curves presented in Fig. 3d indicate that FeCoNiMnRu HEA with the best HER activity among the tested samples, and beating commercial Pt/C at all applied potential window. As seen Fig. 3e, the overpotentials at 10/50/100 mA cm^{-2} for FeCoNiMnRu HEA are merely 36/104/148 mV, which are much lower than those of the FeCoNi (154/263/294 mV), FeCoNiRu (71/174/223 mV) and FeCoNiMn (208/322/366 mV). The Tafel slope of FeCoNiMnRu HEA is determined to be only 41 mV dec^{-1} (Fig. 3f), substantially lower than that of FeCoNi (233 mV dec^{-1}), FeCoNiRu (142 mV dec^{-1}), FeCoNiMn (202 mV dec^{-1}) and Pt/C (53 mV dec^{-1}), thus indicating the faster HER kinetics. Similar to the result observed in alkaline electrolyte, the Tafel slope of FeCoNiMnRu HEA suggests the HER process also follows a Volmer-Heyrovsky mechanism in seawater electrolyte [47]. Moreover, the FeCoNiMnRu HEA possesses the smallest R_{ct} and largest C_{dl} values among all the samples (Fig. S13 and 14), confirming the fastest electron-transfer dynamics and largest ECSA for HER. Moreover, FeCoNiMnRu HEA exhibits the highest ECSA-normalized current density (Fig. S15) and TOF value (Fig. S16) among these HEAs, thus indicating the highest intrinsic HER activity.

Fig. 3g summarizes the overpotential of different HEA-based catalysts for HER in alkaline water/seawater electrolytes. It is worth noting that the overpotentials of FeCoNiMnRu HEA are superior to most recently reported HEA-based catalysts in both alkaline and seawater media (also see Table S1 and S2 for details), further confirming its outstanding HER performance. To examine the stability of FeCoNiMnRu HEA for long-term HER, chronopotentiometry (CP) tests were conducted at the current density of 10/50/100 mA cm^{-2} for 36 h in alkaline water/seawater electrolytes. As shown in Fig. 3h, the FeCoNiMnRu HEA exhibits negligible potential decay during the long-term HER test, implying its remarkable stability. In addition, the SEM and XPS characterizations after stability tests verify that the morphology and composition of the FeCoNiMnRu HEA are well maintained (Fig. S17 and S18), further confirming its excellent stability.

3.3. Interfacial water behavior on FeCoNiMnRu HEA

As known, HER taking place in alkaline water/seawater electrolytes

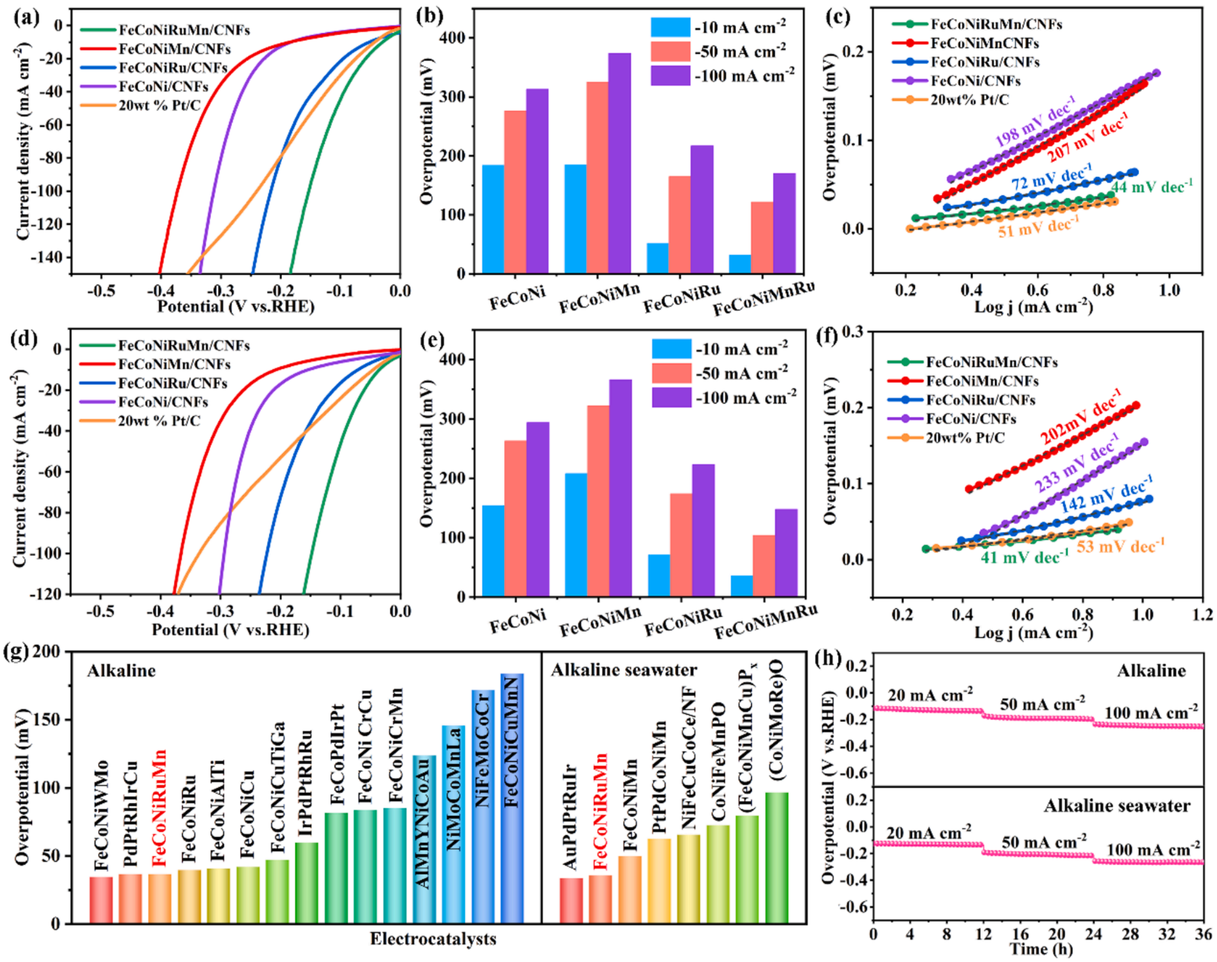

Fig. 3. (a) HER polarization curves, (b) overpotentials at −10/-50/-100 mA cm^{-2}, and (c) Tafel plot of FeCoNi, FeCoNiRu, FeCoNiMn and FeCoNiMnRu in alkaline media. (d) HER polarization curves, (e) overpotentials at −10/-50/-100 mA cm^{-2}, and (f) Tafel plot of FeCoNi, FeCoNiRu, FeCoNiMn and FeCoNiMnRu in seawater media. (g) HER activities of FeCoNiMnRu and reported HEAs in alkaline and seawater media at 10 mA cm^{-2}. (h) V-t curves of FeCoNiMnRu HEA for HER in alkaline and seawater media.

mainly involves two steps, namely the Volmer step ($H_2O + e^- + * \rightarrow H^* + OH^-$) and Heyrovsky ($H^* + H_2O + e^- \rightarrow H_2 + OH^- + *$) or Tafel ($2H^* \rightarrow H_2 + 2^*$) step [48], in which water molecules are the dominant reactant and proton donors. To better understanding the mechanism of HER occurred on HEAs, the behaviors of interfacial water on the surface of FeCoNiMnRu and FeCoNiRu HEAs were systematically investigated through in-situ FTIR. Fig. 4a and b show the in-situ FTIR spectra recorded at potential range from 0.75 to −0.25 V vs. HRE in 1.0 M KOH, in which two distinct spectral bands corresponding to the adsorbed water molecules can be observed on the catalyst surface. The band at ~ 1640 cm^{-1} is assigned to the HOH bending mode of water molecules, while the broad band at 2800 ~ 3750 cm^{-1} is assigned to the O-H stretching mode [22]. Of note, the HOH bending and O-H stretching modes of water molecules adsorbed on the FeCoNiMnRu are respectively redshifted by 5 and 4 cm^{-1} relative to FeCoNiRu, indicating the longer O-H bonds of adsorbed water molecules. The longer O-H bonds suggest the cleavage of water molecules on the FeCoNiMnRu surface would be more easier and accelerate the Volmer step, thus boosting the HER kinetics [49]. Meanwhile, the corresponding contour plots of the in-situ FTIR spectra (Fig. 4c and d) show that the adsorbed water molecules on FeCoNiMnRu surface reach a peak at 0.47 V vs. HRE, which is much higher than that of FeCoNiRu (0.16 V vs. HRE), implying the stronger water adsorption [50]. It is worth mentioning that, the similar phenomena were also observed for FeCoNiMnRu under seawater medium (Fig. S19). Hence, the above results indicate that the surface of FeCoNiMnRu are more favorable to both the adsorption and dissociation of water molecules, confirming the promoted HER kinetics in alkaline water/seawater electrolytes.

Furthermore, we carried out Gaussian fitting on the O-H stretching mode of adsorbed water molecules. As shown in Fig. 4e and f, the O-H stretching mode can be deconvoluted into three components belonging to three types of interfacial water. The bands located at ~ 3200 and 3400 cm^{-1} are assigned to the ice-like symmetric H-bonded water (H_2O-sym) and liquid-like asymmetric H-bonded water (H_2O-asym), respectively, while the band located at ~ 3570 cm^{-1} is attributed to the weak H-bonded water (H_2O-free) [22]. Specifically, the vibrational frequency of H_2O-sym, H_2O-asym and H_2O-free on FeCoNiMnRu are found to be located at 3213, 3391 and 3556 cm^{-1}, respectively. Notably, the vibrational frequency of H_2O-free on FeCoNiMnRu is much lower than that of FeCoNiRu (3587 cm^{-1}), further confirming the stronger interaction with water molecules, which would facilitate the break of the O-H bond of adsorbed water [51]. Moreover, Fig. 4g shows that the proportion of H_2O-free on FeCoNiMnRu increases rapidly from 7.1 % to 10.5 % with the potential decreased from 0.75 to −0.25 V vs. HRE, achieving an increasing rate of 8.85 % V^{-1}. In contrary, the proportion of H_2O-free on FeCoNiRu with decreased potential leads to an increasing rate of only 2.91 % V^{-1}. Similarly, Fig. S20 shows that the fast increasing rate of H_2O-free on surface of FeCoNiMnRu is further verified in seawater electrolyte. It is worth noting that the proportion of H_2O-free in the interfacial water increases with the decreased potential suggests that

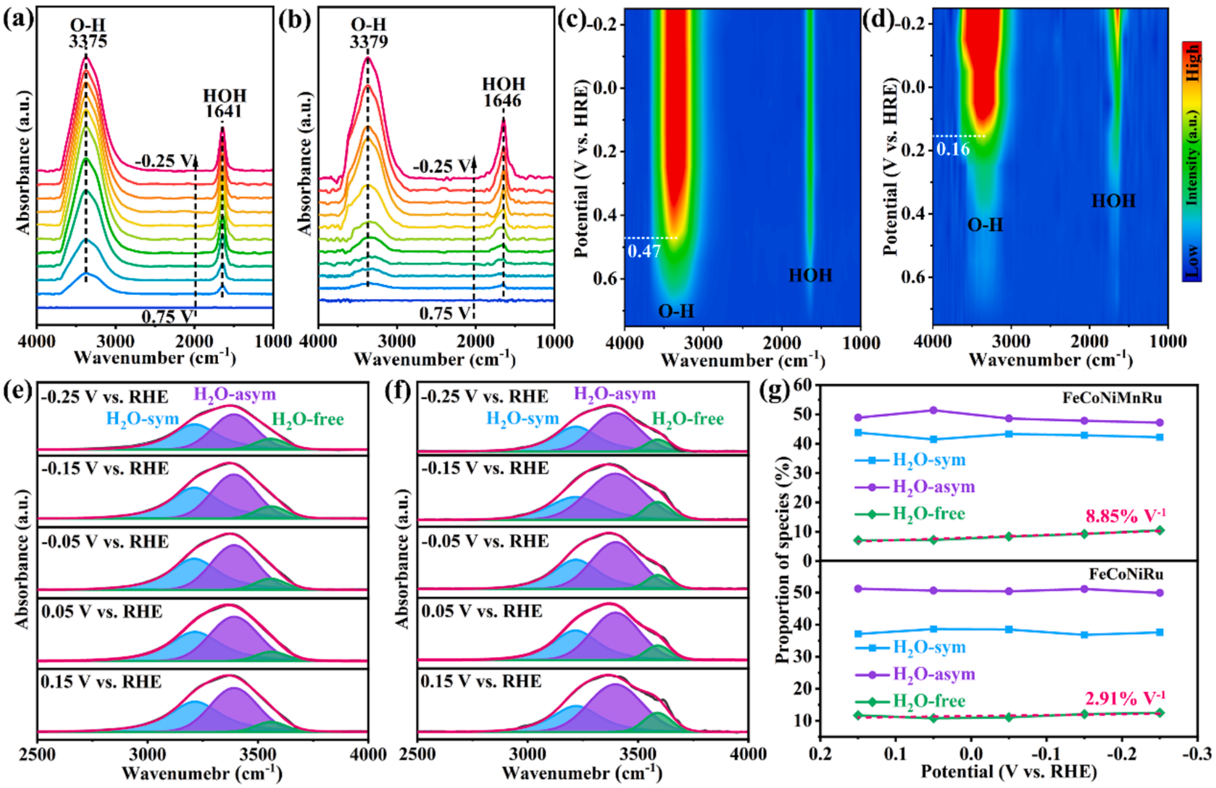

Fig. 4. In-situ FTIR spectra and corresponding contour plots of (a, c) FeCoNiMnRu and (b, d) FeCoNiRu under different potentials in 1.0 M KOH. In-situ FTIR spectra of interfacial water at surface of (e) FeCoNiMnRu and (f) FeCoNiRu under 0.15 V to −0.25 V vs. RHE in 1.0 M KOH. (g) The proportion of interfacial water configurations on surface of FeCoNiMnRu and FeCoNiRu at 0.15 V to −0.25 V vs. RHE derived from the FTIR spectra in (e, f).

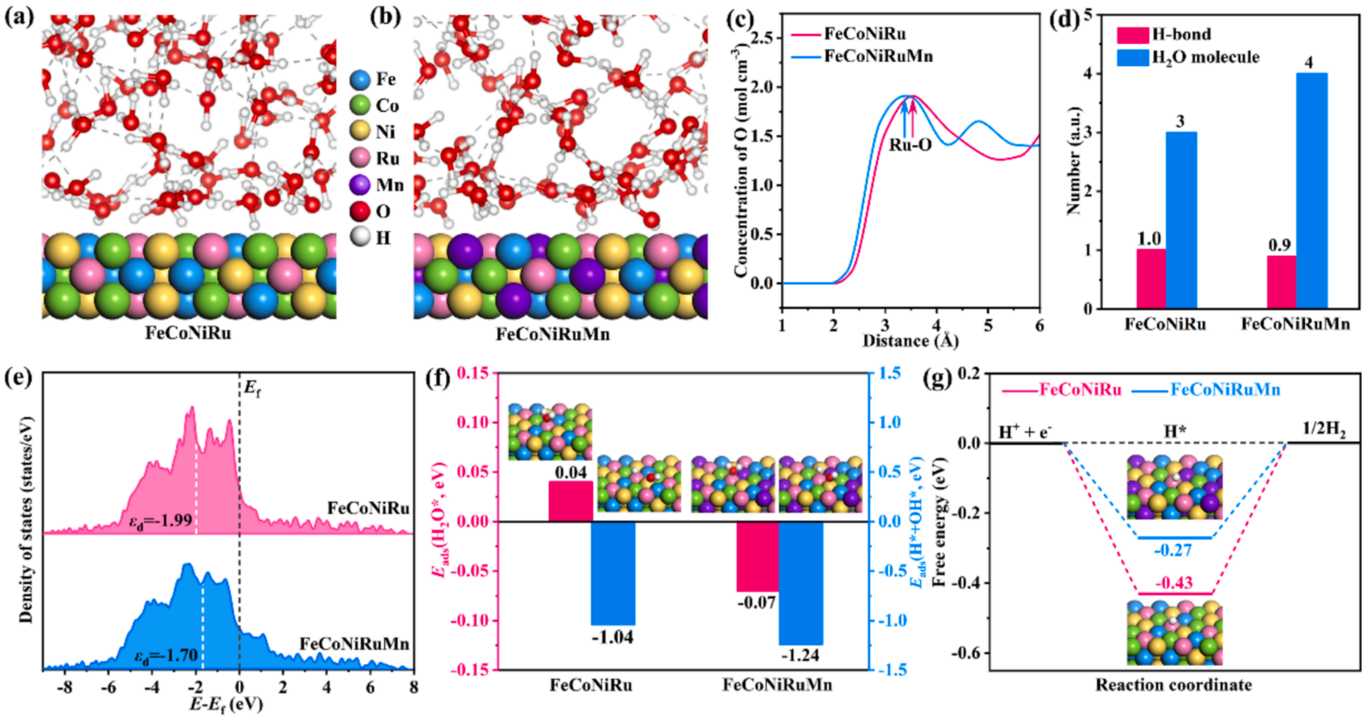

Fig. 5. Representative snapshots of the interfacial water structures near the surface of (a) FeCoNiRu and (b) FeCoNiMnRu. (c) The concentration profiles of O atom in H_2O molecules along the vertical surface of FeCoNiRu and FeCoNiMnRu. (d) The average number of H-bond per H_2O molecule and the corresponding number of H_2O molecules on the surface of FeCoNiRu and FeCoNiMnRu. (e) Calculated PDOS and *d*-band center of FeCoNiRu and FeCoNiMnRu. (f) Calculated adsorption energy of $E_{ads}(H_2O^*)$ and $E_{ads}(H^*+OH^*)$ on FeCoNiRu and FeCoNiMnRu. (g) Calculated hydrogen adsorption free energy (ΔG_{H^*}) of Ru sites in FeCoNiRu and FeCoNiMnRu.

there is a process of converting H_2O-sym and H_2O-asym to H_2O-free [52]. Since the H_2O-free is the direct reactant of Volmer process, the rapid conversion of H_2O-sym/H_2O-asym to H_2O-free would boost the Volmer step and generate more protons for the active sites to participate in the subsequent Heyrovsky or Tafel steps, which consequently promotes the HER performance [53]. In this regard, the FeCoNiMnRu HEA with fast H_2O-free conversion rate obviously increases the number of available/active H_2O^* to the active sites, thus facilitating the enhanced HER activity. The above in-situ FTIR spectra results illustrate that the introduced Mn element and defect-rich structure effectively optimize the interfacial water structure of FeCoNiMnRu HEA. The optimized interfacial water structure of FeCoNiMnRu HEA not only facilitates the adsorption and dissociation of water molecules, but also contributes to the generation of more free water under negative potential to participate the surface HER process, thereby accounting for the boosted HER performance observed in the polarization curves (Fig. 3a and d).

3.4. HER mechanisms on FeCoNiMnRu HEA

Interfacial water is the most important participant in HER, understanding the water/catalyst interface structure is crucial to disclosing the underlying mechanism of HER. To unveil the structure of interfacial water on catalyst surface, we employed AIMD calculations to explore the structure of interfacial water on surfaces of FeCoNiRu and FeCoNiMnRu HEAs. Fig. 5a and b present the pepresentative snapshots of the water molecules on the (111) facets of FeCoNiRu and FeCoNiMnRu, respectively. To probe the distributions of interfacial water molecules, we carried out the oxygen concentration profiles along the vertical direction of (111) facets. As shown in Fig. 5c, we found that the nearest distance between O atoms in water molecules and Ru atoms in FeCoNiRu and FeCoNiMnRu is measured to be 2.02 and 1.95 Å, respectively. Of note, these distances for Ru-O atoms are very similar to that of the Ru-O valence bond in RuO_2 (1.98 Å) [54], implying some adsorbed water molecules within the firstly layer present chemisorbed characters. Meanwhile, the first concentration peak appears with the Ru-O distance of 3.55 and 3.37 Å for FeCoNiRu and FeCoNiMnRu, respectively. Obviously, the Ru-O interatomic distance on the FeCoNiMnRu surface is decreased compared with that of FeCoNiRu, suggesting the strong absorption with the water molecules, consistent well with the in-situ FTIR results (Fig. 4c and d). Fig. 5d shows the calculated number of hydrogen bonds (H-bonds) per water molecule and water molecules within the interfacial region. As seen that the average number of H-bonds per interfacial water on FeCoNiRu and FeCoNiMnRu are determined to be 1.0 and 0.9, and the corresponding numbers of water molecules are 3 and 4, respectively. The FeCoNiMnRu has a smaller average number of H-bonds per interfacial water while larger number of water molecules, indicating the more disordered H-bond network and higher interfacial water concentration. It is worth mentioning that the disordered H-bond network of interfacial water is conductive to both the transfer of H_2O^*/OH^* and the availability of H_2O^* at the active sites, thereby accelerating the HER kinetics and efficiency [22,55].

DFT calculations were then carried out to disclose the correlation between the electronic structures and HER activities of FeCoNiMnRu HEA. Given the *d*-electron configurations of electrocatalysts greatly dominate the electrocatalytic reactions [56], the *d*-orbital projected density of states (DOSs) of FeCoNiRu and FeCoNiMnRu HEAs were firstly calculated. As illustrated in Fig. 5e, the *d*-orbital of FeCoNiMnRu HEA shows apparently higher occupied state than the FeCoNiRu near the Fermi level (E_f), indicating the stronger hybridization occurred within the FeCoNiMnRu HEA. The more dominated *d*-electron near the E_f for FeCoNiMnRu HEA not only endows the faster electron transfer, but also induce more free-electrons near active sites and thus facilitating the catalysis of the HER. Meanwhile, the *d*-band center of FeCoNiRu and FeCoNiMnRu is determined to be −1.70 and −1.99 eV, respectively. Obviously, FeCoNiMnRu HEA has a closer *d*-band center towards E_f than that of FeCoNiRu, which would favor the adsorption of the H_2O molecules and stabilization of H^*/OH^* intermediates [47]. Fig. 5f shows the adsorption energy of water $E_{ads}(H_2O^*)$ and dissociative configuration $E_{ads}(H^*{+}OH^*)$ on the surface of FeCoNiRu and FeCoNiMnRu HEAs. It is found that the $E_{ads}(H_2O^*)$ values on the FeCoNiRu and FeCoNiMnRu surfaces are calculated to be 0.04 and −0.07 eV, respectively. This suggests that the surface of FeCoNiMnRu has a stronger adsorption ability for water molecules, which is consistent with the results observed in the in-situ FTIR spectra (Fig. 4a-d). For dissociative adsorption, the $E_{ads}(H^*{+}OH^*)$ on the surface of FeCoNiRu and FeCoNiMnRu HEAs is calculated to be −1.04 and −1.24 eV, respectively. The $E_{ads}(H^*{+}OH^*)$ value on the surface of FeCoNiMnRu HEA is more negative than that of FeCoNiRu, implying the former has strong adsorption of the $H^*{+}OH^*$ species. This result also signifies that FeCoNiMnRu HEA is able to offer an effective destabilization of the H-OH bond [55], and thus facilitating the water dissociation. The calculated free energy values of adsorption H^* (ΔG_{H^*}) on FeCoNiRu and FeCoNiMnRu HEAs were presented in Fig. 5g. As seen that the ΔG_{H^*} value on Ru site in FeCoNiRu is calculated to be −0.43 eV, indicating the strong hydrogen adsorption. By contrast, the Ru site in FeCoNiMnRu HEA achieves a more appropriate ΔG_{H^*} value of −0.24 eV, implying the higher intrinsic HER activity theoretically.

4. Conclusions

In summary, we have successfully developed a defect-rich FeCoNiMnRu HEA by rapid Joule-heating approach, which could significantly activate the rigid interfacial water and boost the HER kinetics and efficiency. The developed defect-rich FeCoNiMnRu HEA delivered excellent HER activity with overpotentials of only 37 and 35 mV at 10 mA cm^{-2} in alkaline water and seawater electrolyte, respectively. Combing in-situ FTIR and theoretical calculations, we confirmed that the constructed FeCoNiMnRu HEA endows a discorded interfacial water structure, which facilitates the conversion of interfacial water from strong H-bonded water to free water, thus increasing the availability and activity of interfacial water at the active sites and accounting for the boosted HER performance observed experimentally. Our findings demonstrated that HEAs with optimized composition and structure could effectively active the rigid interface water and promote the HER kinetics and efficiency, thus providing novel paradigm for designing advanced HEA-based catalysts.

CRediT authorship contribution statement

Guangbo Liu: Writing – original draft, Validation, Methodology, Funding acquisition, Formal analysis. **Chen Song:** Methodology, Investigation, Formal analysis, Data curation. **Xiaolei Li:** Validation, Resources, Formal analysis. **Qisen Jia:** Methodology, Data curation. **Pengfei Wu:** Validation, Software. **Zhihao Lou:** Investigation. **Yuanshuo Ma:** Methodology. **Xuejing Cui:** Resources. **Xin Zhou:** Writing – review & editing, Software, Funding acquisition, Formal analysis. **Luhua Jiang:** Writing – review & editing, Supervision, Project administration, Funding acquisition, Formal analysis.

Declaration of competing interest

The authors declare that they have no known competing financial interests or personal relationships that could have appeared to influence the work reported in this paper.

Acknowledgments

This work was financially supported by National Natural Science Foundation of China (22279069, 22179067, 22372017 and 22478211) and Major Fundamental Research Program of Natural Science Foundation of Shandong Province (ZR2022ZD10).

Appendix A. Supplementary data

Supplementary data to this article can be found online at https://doi.org/10.1016/j.cej.2025.161070.

Data availability

Data will be made available on request.

References

[1] H. Zhao, Z.Y. Yuan, Progress and perspectives for solar-driven water electrolysis to produce green hydrogen, Adv. Energy Mater. 13 (2023) 2300254.

[2] X. Liu, J. Chi, H. Mao, L. Wang, Principles of designing electrocatalyst to boost reactivity for seawater splitting, Adv. Energy Mater. 13 (2023) 2301438.

[3] A.A. Feidenhansl, Y.N. Regmi, C. Wei, D. Xia, J. Kibsgaard, L.A. King, Precious metal free hydrogen evolution catalyst design and application, Chem. Rev. 124 (2024) 5617–5667.

[4] G. Liu, Y. Xu, T. Yang, L. Jiang, Recent advances in electrocatalysts for seawater splitting, Nano Mater. Sci. 5 (2023) 101–116.

[5] K.N. Dinh, Q. Liang, C.-F. Du, J. Zhao, A.I.Y. Tok, H. Mao, Q. Yan, Nanostructured metallic transition metal carbides, nitrides, phosphides, and borides for energy storage and conversion, Nano Today 25 (2019) 99–121.

[6] Y. Hu, M. Tu, T. Xiong, Y. He, M. Mushtaq, H. Yang, Z. Khanam, Y. Huang, J. Deng, M.S. Balogun, Thermal strain engineering in cobalt-coordinated Mo_2N for efficient ampere-level current density alkaline fresh/seawater hydrogen evolution electrocatalysis, Journal of Energy Chemistry 103 (2025) 282–293.

[7] J. Li, Z. Zhu, Y. Huang, F. Wang, M.-S. Balogun, Ni_3N: A multifunctional material for energy storage and electrocatalysis, Mater. Today Energy 26 (2022) 101001.

[8] Z. Zhu, L. Luo, Y. He, M. Mushtaq, J. Li, H. Yang, Z. Khanam, J. Qu, Z. Wang, M.-S. Balogun, High-performance alkaline freshwater and seawater hydrogen catalysis by sword-head structured Mo_2N-Ni_3Mo_3N tunable interstitial compound electrocatalysts, Adv. Funct. Mater. 34 (2024) 2306061.

[9] Y. Saira, Z. Li, Y. Zhu, Q. Liu, W. Luo, Y. Wang, M. Gong, G. Fu, Y. Tang, Low-loaded Ru on hollow SnO_2 for enhanced electrocatalytic hydrogen evolution, Chem. Commun. 60 (2024) 2768–2771.

[10] T.A.A. Batchelor, J.K. Pedersen, S.H. Winther, I.E. Castelli, K.W. Jacobsen, J. Rossmeisl, High-entropy alloys as a discovery platform for electrocatalysis, Joule 3 (2019) 834–845.

[11] Y. Xin, S. Li, Y. Qian, W. Zhu, H. Yuan, P. Jiang, R. Guo, L. Wang, High-entropy alloys as a platform for catalysis: Progress, challenges, and opportunities, ACS Catal. 10 (2020) 11280–11306.

[12] Z.-J. Zhang, N. Yu, Y.-L. Dong, G. Han, H. Hu, Y.-M. Chai, B. Dong, High entropy catalysts in electrolytic water splitting: A review from properties to applications, Chem. Eng. J. 498 (2024) 155736.

[13] J. Hao, Z. Zhuang, K. Cao, G. Gao, C. Wang, F. Lai, S. Lu, P. Ma, W. Dong, T. Liu, M. Du, H. Zhu, Unraveling the electronegativity-dominated intermediate adsorption on high-entropy alloy electrocatalysts, Nat. Commun. 13 (2022) 2662.

[14] X. Zou, J. Xie, Z. Mei, Q. Jing, X. Sheng, C. Zhang, Y. Yang, M. Sun, F. Ren, L. Wang, T. He, Y. Kong, H. Guo, High-entropy engineering with regulated defect structure and electron interaction tuning active sites for trifunctional electrocatalysis, Proc. Natl. Acad. Sci. 121 (2024) e2313239121.

[15] Y. Yang, Z. Jia, Q. Wang, Y. Liu, L. Sun, B. Sun, J. Kuang, S. Dai, J. He, S. Liu, L. Duan, H. Tang, L.-C. Zhang, J.J. Kruzic, J. Lu, B. Shen, Vacancy induced microstrain in high-entropy alloy film for sustainable hydrogen production under universal pH conditions, Energ. Environ. Sci. 17 (2024) 5854–5865.

[16] Y. Yao, Q. Dong, A. Brozena, J. Luo, J. Miao, M. Chi, C. Wang, I.G. Kevrekidis, Z. J. Ren, J. Greeley, G. Wang, A. Anapolsky, L. Hu, High-entropy nanoparticles: Synthesis-structure-property relationships and data-driven discovery, Science 376 (2022) eabn3103.

[17] J.-T. Ren, L. Chen, H.-Y. Wang, Z.-Y. Yuan, High-entropy alloys in electrocatalysis: from fundamentals to applications, Chem. Soc. Rev. 52 (2023) 8319–8373.

[18] Y.-H. Wang, S. Zheng, W.-M. Yang, R.-Y. Zhou, Q.-F. He, P. Radjenovic, J.-C. Dong, S. Li, J. Zheng, Z.-L. Yang, G. Attard, F. Pan, Z.-Q. Tian, J.-F. Li, In situ Raman spectroscopy reveals the structure and dissociation of interfacial water, Nature 600 (2021) 81–85.

[19] Y. Tian, B. Huang, Y. Song, Y. Zhang, D. Guan, J. Hong, D. Cao, E. Wang, L. Xu, Y. Shao-Horn, Y. Jiang, Effect of ion-specific water structures at metal surfaces on hydrogen production, Nat. Commun. 15 (2024) 7834.

[20] P. Li, Y. Jiang, Y. Hu, Y. Men, Y. Liu, W. Cai, S. Chen, Hydrogen bond network connectivity in the electric double layer dominates the kinetic pH effect in hydrogen electrocatalysis on Pt, Nat. Catal. 5 (2022) 900–911.

[21] X. Chen, L. Chen, C. Chen, D. Shi, J. Song, Y. Qin, X. Wang, M.M. Amjad, D. Sun, B. Sun, K. Zhang, Rational design of dynamic interface water evolution on turing electrocatalyst toward the industrial hydrogen production, Adv. Mater. 36 (2024) 2401110.

[22] K. Sun, X. Wu, Z. Zhuang, L. Liu, J. Fang, L. Zeng, J. Ma, S. Liu, J. Li, R. Dai, X. Tan, K. Yu, D. Liu, W.-C. Cheong, A. Huang, Y. Liu, Y. Pan, H. Xiao, C. Chen, Interfacial water engineering boosts neutral water reduction, Nat. Commun. 13 (2022) 6260.

[23] M. Wang, K. Sun, W. Mi, C. Feng, Z. Guan, Y. Liu, Y. Pan, Interfacial water activation by single-atom Co–N_3 sites coupled with encapsulated Co nanocrystals for accelerating electrocatalytic hydrogen evolution, ACS Catal. 12 (2022) 10771–10780.

[24] L. Zhang, H. Hu, C. Sun, D. Xiao, H.-T. Wang, Y. Xiao, S. Zhao, K.H. Chen, W.-X. Lin, Y.-C. Shao, X. Wang, C.-W. Pao, L. Han, Bimetallic nanoalloys planted on super-hydrophilic carbon nanocages featuring tip-intensified hydrogen evolution electrocatalysis, Nat. Commun. 15 (2024) 7179.

[25] Y. Zhu, X. Wu, Z. Wu, X. Wang, X. Wang, C. Wang, X. Zhu, M. Li, D. Sun, H. Li, Y. Tang, G. Fu, Europium oxide evoked multisite synergism to facilitate water dissociation for alkaline hydrogen evolution, Adv. Funct. Mater. 34 (2024) 2409324.

[26] M. Li, X. Wang, H. Du, W. Dong, S. Ye, H. Liu, H. Sun, K. Huang, H. Li, Y. Tang, G. Fu, Oxophilic Tm-sites in MoS_2 trigger thermodynamic spontaneous water dissociation for enhanced hydrogen evolution, Adv. Energy Mater. 14 (2024) 2401716.

[27] D. Liu, X. Li, S. Chen, H. Yan, C. Wang, C. Wu, Y.A. Haleem, S. Duan, J. Lu, B. Ge, P. M. Ajayan, Y. Luo, J. Jiang, L. Song, Atomically dispersed platinum supported on curved carbon supports for efficient electrocatalytic hydrogen evolution, Nat. Energy 4 (2019) 512–518.

[28] G. Kresse, J. Furthmüller, Efficiency of ab-initio total energy calculations for metals and semiconductors using a plane-wave basis set, Comput. Mater. Sci 6 (1996) 15–50.

[29] G. Kresse, J. Furthmüller, Efficient iterative schemes for ab initio total-energy calculations using a plane-wave basis set, Phys. Rev. B 54 (1996) 11169–11186.

[30] P.E. Blöchl, Projector augmented-wave method, Phys. Rev. B 50 (1994) 17953–17979.

[31] J.P. Perdew, K. Burke, M. Ernzerhof, Generalized gradient approximation made simple, Phys. Rev. Lett. 77 (1996) 3865–3868.

[32] A. Zunger, S.H. Wei, L.G. Ferreira, J.E. Bernard, Special quasirandom structures, Phys. Rev. Lett. 65 (1990) 353–356.

[33] A. van de Walle, M. Asta, G. Ceder, The alloy theoretic automated toolkit: A user guide, Calphad 26 (2002) 539–553.

[34] J.K. Nørskov, T. Bligaard, A. Logadottir, J.R. Kitchin, J.G. Chen, S. Pandelov, U. Stimming, Trends in the exchange current for hydrogen evolution, J. Electrochem. Soc. 152 (2005) J23.

[35] S. Nosé, A unified formulation of the constant temperature molecular dynamics methods, J. Chem. Phys. 81 (1984) 511–519.

[36] W.G. Hoover, Canonical dynamics: Equilibrium phase-space distributions, Phys. Rev. A 31 (1985) 1695–1697.

[37] Y. Xie, S. Xu, A.C. Meng, B. Zheng, Z. Chen, J.M. Tour, J. Lin, Laser-induced high-entropy alloys as long-duration bifunctional electrocatalysts for seawater splitting, Energ. Environ. Sci. 17 (2024) 8670–8682.

[38] X. Cui, Y. Liu, X. Wang, X. Tian, Y. Wang, G. Zhang, T. Liu, J. Ding, W. Hu, Y. Chen, Rapid high-temperature liquid shock synthesis of high-entropy alloys for hydrogen evolution reaction, ACS Nano 18 (2024) 2948–2957.

[39] Y. Xu, Y. Fo, H. Lv, X. Cui, G. Liu, X. Zhou, L. Jiang, Anderson-type polyoxometalate-assisted synthesis of defect-rich doped 1T/2H-$MoSe_2$ nanosheets for efficient seawater splitting and Mg/seawater batteries, ACS Appl. Mater. Interfaces 14 (2022) 10246–10256.

[40] Q. Quan, X. Li, C. Song, Q. Jia, H. Lu, X. Cui, G. Liu, X. Chen, L. Jiang, Polyoxometalate-derived bi-functional crystalline/amorphous interfaces with optimized d-electron configuration for efficient self-powered hydrazine-seawater splitting, Chem. Eng. J. 488 (2024) 150897.

[41] G. Liu, H. Lv, Q. Quan, X. Li, H. Lu, W. Li, X. Cui, L. Jiang, Self-powered electrolysis systems for sustainable hydrogen generation from natural seawater via a Ni/V_2O_3 Schottky electrode, Chem. Eng. J. 450 (2022) 138079.

[42] M.C. Biesinger, B.P. Payne, A.P. Grosvenor, L.W.M. Lau, A.R. Gerson, R.S.C. Smart, Resolving surface chemical states in XPS analysis of first row transition metals, oxides and hydroxides: Cr, Mn, Fe, Co and Ni, Appl. Surf. Sci. 257 (2011) 2717–2730.

[43] X. Xu, Y. Guo, B.P. Bloom, J. Wei, H. Li, H. Li, Y. Du, Z. Zeng, L. Li, D.H. Waldeck, Elemental core level shift in high entropy alloy nanoparticles via X-ray photoelectron spectroscopy analysis and first-principles calculation, ACS Nano 14 (2020) 17704–17712.

[44] Y. Xu, H. Lv, H. Lu, Q. Quan, W. Li, X. Cui, G. Liu, L. Jiang, Mg/seawater batteries driven self-powered direct seawater electrolysis systems for hydrogen production, Nano Energy 98 (2022) 107295.

[45] T. Yang, H. Lv, Q. Quan, X. Li, H. Lu, X. Cui, G. Liu, L. Jiang, Electronic structure modulation of MoO_2 via Er-doping for efficient overall water/seawater splitting and Mg/seawater batteries, Appl. Surf. Sci. 615 (2023) 156360.

[46] T. Xiong, Z. Zhu, Y. He, M.-S. Balogun, Y. Huang, Phase evolution on the hydrogen adsorption kinetics of NiFe-based heterogeneous catalysts for efficient water electrolysis, Small Methods 7 (2023) 2201472.

[47] G. Liu, S. Liu, X. Li, H. Lv, H. Qu, Q. Quan, H. Lu, X. Cui, X. Zhou, L. Jiang, J. Qiu, Optimized W-d band configuration in porous sodium tungsten bronze octahedron enabling Pt-like and wide-pH hydrogen evolution, Nano Energy 123 (2024) 109442.

[48] Z. Zhou, Z. Pei, L. Wei, S. Zhao, X. Jian, Y. Chen, Electrocatalytic hydrogen evolution under neutral pH conditions: current understandings, recent advances, and future prospects, Energ. Environ. Sci. 13 (2020) 3185–3206.

[49] X. Wu, S. Zhou, Z. Wang, J. Liu, W. Pei, P. Yang, J. Zhao, J. Qiu, Engineering multifunctional collaborative catalytic interface enabling efficient hydrogen evolution in all pH range and seawater, Adv. Energy Mater. 9 (2019) 1901333.

[50] X. Liu, S. Wei, S. Cao, Y. Zhang, W. Xue, Y. Wang, G. Liu, J. Li, Lattice strain with stabilized oxygen vacancies boosts ceria for robust alkaline hydrogen evolution outperforming benchmark pt, Adv. Mater. 36 (2024) 2405970.

[51] X. Chen, X.-T. Wang, J.-B. Le, S.-M. Li, X. Wang, Y.-J. Zhang, P. Radjenovic, Y. Zhao, Y.-H. Wang, X.-M. Lin, J.-C. Dong, J.-F. Li, Revealing the role of interfacial

water and key intermediates at ruthenium surfaces in the alkaline hydrogen evolution reaction, Nat. Commun. 14 (2023) 5289.

[52] S. Wang, T. Jiang, Y. Hao, J. Wu, C. Lei, Z. Chen, W. Du, M. Gong, Unveiling the cation dependence in alkaline hydrogen evolution by differently-charged ruthenium/molybdenum sulfide hybrids, Adv. Mater. 36 (2024) 2410422.

[53] L.-F. Shen, B.-A. Lu, Y.-Y. Li, J. Liu, Z.-C. Huang-fu, H. Peng, J.-Y. Ye, X.-M. Qu, J.-M. Zhang, G. Li, W.-B. Cai, Y.-X. Jiang, S.-G. Sun, Interfacial structure of water as a new descriptor of the hydrogen evolution reaction, Angew. Chem. Int. Ed. 59 (2020) 22397–22402.

[54] Y. Yang, J. Guo, L. Xu, C. Li, R. Ning, J. Ma, S. Geng, Bond engineering: weakening Ru–O covalency for efficient and stable water oxidation in acidic solutions, Journal of Energy Chemistry 102 (2025) 1–9.

[55] X.H. Chen, X.L. Li, T. Li, J.H. Jia, J.L. Lei, N.B. Li, H.Q. Luo, Enhancing neutral hydrogen production by disrupting the rigid hydrogen bond network on Ru nanoclusters through Nb_2O_5-mediated water reorientation, Energ. Environ. Sci. 17 (2024) 5091–5101.

[56] J.K. Nørskov, F. Abild-Pedersen, F. Studt, T. Bligaard, Density functional theory in surface chemistry and catalysis, Proc. Natl. Acad. Sci. 108 (2011) 937–943.